



Publication Year	2015
Acceptance in OA @INAF	2020-04-09T14:21:22Z
Title	The Swift X-Ray Telescope Cluster Survey. III. Cluster Catalog from 2005-2012 Archival Data
Authors	Liu, Teng; TOZZI, Paolo; Tundo, Elena; MORETTI, Alberto; Rosati, Piero; et al.
DOI	10.1088/0067-0049/216/2/28
Handle	http://hdl.handle.net/20.500.12386/23966
Journal	THE ASTROPHYSICAL JOURNAL SUPPLEMENT SERIES
Number	216

THE *SWIFT* X-RAY TELESCOPE CLUSTER SURVEY. III. CLUSTER CATALOG FROM 2005–2012 ARCHIVAL DATA

TENG LIU (刘腾)¹, PAOLO TOZZI², ELENA TUNDO², ALBERTO MORETTI³, PIERO ROSATI⁴, JUN-XIAN WANG¹,
GIANPIERO TAGLIAFERRI⁵, SERGIO CAMPANA⁵, AND MAURO GIAVALISCO⁶

¹ CAS Key Laboratory for Research in Galaxies and Cosmology, Department of Astronomy,
University of Science and Technology of China, 230026 Hefei, Anhui, China; liuteng@ustc.edu.cn

² INAF, Osservatorio Astrofisico di Firenze, Largo Enrico Fermi 5, I-50125 Firenze, Italy

³ INAF, Osservatorio Astronomico di Brera, Via Brera 28, I-20121 Milano, Italy

⁴ Università degli Studi di Ferrara, Dipartimento di Fisica e Scienze della Terra, Via Saragat 1, I-44121 Ferrara, Italy

⁵ INAF, Osservatorio Astronomico di Brera, Via Bianchi 46, I-23807 Merate (LC), Italy

⁶ Department of Astronomy, University of Massachusetts, LGRT-B 619E, 710 North Pleasant Street, Amherst, MA, USA

Received 2014 October 3; accepted 2014 December 16; published 2015 January 27

ABSTRACT

We present the *Swift* X-ray Cluster Survey (SWXCS) catalog obtained using archival data from the X-ray telescope (XRT) on board the *Swift* satellite acquired from 2005 February to 2012 November, extending the first release of the SWXCS. The catalog provides positions, soft fluxes, and, when possible, optical counterparts for a flux-limited sample of X-ray group and cluster candidates. We consider the fields with Galactic latitude $|b| > 20^\circ$ to avoid high H I column densities. We discard all of the observations targeted at groups or clusters of galaxies, as well as particular extragalactic fields not suitable to search for faint extended sources. We finally select ~ 3000 useful fields covering a total solid angle of ~ 400 deg². We identify extended source candidates in the soft-band (0.5–2 keV) images of these fields using the software *EXSDetect*, which is specifically calibrated for the XRT data. Extensive simulations are used to evaluate contamination and completeness as a function of the source signal, allowing us to minimize the number of spurious detections and to robustly assess the selection function. Our catalog includes 263 candidate galaxy clusters and groups down to a flux limit of 7×10^{-15} erg cm⁻² s⁻¹ in the soft band, and the $\log N$ - $\log S$ is in very good agreement with previous deep X-ray surveys. The final list of sources is cross-correlated with published optical, X-ray, and Sunyaev–Zeldovich catalogs of clusters. We find that 137 sources have been previously identified as clusters in the literature in independent surveys, while 126 are new detections. Currently, we have collected redshift information for 158 sources (60% of the entire sample). Once the optical follow-up and the X-ray spectral analysis of the sources are complete, the SWXCS will provide a large and well-defined catalog of groups and clusters of galaxies to perform statistical studies of cluster properties and tests of cosmological models.

Key words: catalogs – cosmology: observations – galaxies: clusters: general – surveys – X-rays: galaxies: clusters

Supporting material: machine-readable tables

1. INTRODUCTION

Groups and clusters of galaxies are the most massive, gravitationally bound structures in the universe and their hot intra-cluster medium (ICM) makes them appear as prominent extended sources in the X-ray sky. Therefore, X-ray cluster surveys are among the most efficient tools for constraining cosmological parameters and primordial density fluctuations. A large and complete catalog of groups and galaxy clusters spanning a wide range of redshifts would be crucial to make significant steps toward the understanding of cosmic structure formation and evolution (Rosati et al. 2002a; Schuecker 2005; Voit 2005; Borgani 2008), the chemical and thermodynamical cosmic history of the ICM (Ettori et al. 2004; Balestra et al. 2007; Maughan et al. 2008; Anderson et al. 2009), and to provide an accurate measurement of cosmological parameters (see Vikhlinin et al. 2009; Mantz et al. 2010; Allen et al. 2011).

However, this task is not within the scope of current X-ray missions. None of the major X-ray facilities existing today were designed for surveys, and they have a low efficiency when discovering rare objects like galaxy clusters, particularly at high redshifts. The main characteristics required for an effective X-ray survey mission for extended sources are the following: large field of view (FOV; of the order of 1 deg²), high angular resolution (of the order of a few arcseconds), low background,

and a large effective area (of the order of 10⁴ cm²). Looking at the near future, the upcoming mission *eROSITA* (Predehl et al. 2010; Merloni et al. 2012) will finally provide an X-ray all-sky coverage 20 years after the *ROSAT* All Sky Survey (Voges et al. 1999), down to limiting fluxes more than one order of magnitude deeper than *ROSAT* for extended sources. Therefore *eROSITA* will considerably increase the number of X-ray groups and clusters particularly at low and moderate redshifts. However, its limiting flux is predicted to be $\sim 3.4 \times 10^{-14}$ erg cm⁻² s⁻¹ after four years of operation, well above the level below which the majority of the high- z clusters, and medium- and high- z groups, are currently found. In addition, its low effective area above 2 keV severely limits the characterization of the ICM in high-temperature clusters (see Borm et al. 2014).

Currently, the best resource for building X-ray cluster samples is provided by the still increasing archives of the major X-ray facilities *Chandra* and *XMM-Newton*. For a review of the ongoing X-ray cluster surveys, up to the year 2012, see Table 1 in Tundo et al. (2012). In this framework, we recently presented the *Swift* X-ray Cluster Survey (SWXCS; Tundo et al. 2012, hereafter Paper I), which is based on the archival data of the X-ray telescope (XRT; Burrows et al. 2005) on board the *Swift* satellite (Gehrels et al. 2004). Despite its small collecting area (about one-fifth of *Chandra*), XRT has two characteristics which make it an efficient instrument for the detection and characterization of

extended sources: a low background (Moretti et al. 2009) and a constant angular resolution (with a half energy width of $\text{HEW} = 18''$) across the entire FOV (Moretti et al. 2007). We note that the XRT angular resolution is as good as the resolution of *XMM-Newton* at the aimpoint, and therefore better than *XMM-Newton* when averaged over the FOV. The first catalog of the SWXCS project, including 72 clusters and groups, was presented in Paper I, while the X-ray spectral analysis for more than half of this sample is presented in Tozzi et al. (2014, hereafter Paper II).

In Paper I, we used only the gamma-ray burst (GRB) follow-up observations of XRT released before 2010 April. The sample we built in Paper I has demonstrated the efficiency of an X-ray telescope as small as XRT for finding and characterizing X-ray extended sources. The natural next step is the inclusion of the entire *Swift*-XRT archive, which is the goal of this work. With this aim, we developed software designed for the detection and photometry of extended sources and optimized for the characteristics of XRT data (*EXSdetect*, Liu et al. 2013). The source detection method used in *EXSdetect* is a combination of Voronoi Tessellation and friend-of-friend algorithms (VT+FOF, Ebeling & Wiedenmann 1993). This method does not require a priori assumptions about the shape and size of the sources, and it is particularly efficient when applied to X-ray images characterized by many empty pixels. Its main limitation consists in the blending effect of merging neighboring sources into one. Spurious extended sources may occur due to the bridging of two or more faint unresolved sources, or to the overlap of true extended emission with the wings of bright, unresolved sources. To mitigate this effect, in *EXSdetect* we developed an accurate deblending procedure which is very effective for identifying and separating most of the blended sources, and eventually removing the unresolved sources mistakenly included within extended emission.

The efficiency of our detection algorithm as a function of the exposure time and the source flux, and the accuracy in the source photometry, are investigated by extensive imaging simulations. Most importantly, our simulations allow us to evaluate the contamination (number of spurious extended sources) and the completeness of the catalog as a function of the source flux. In the simulations, we make use of an empirical model of the point-spread function (PSF) of XRT. Thanks to our simulations, we can identify an optimal threshold in the source photometry above which our catalog reaches the required completeness and purity. This threshold directly provides a position-dependent flux limit for each field, and hence a selection function depending on the physical source flux for the entire survey. This step is particularly relevant since, once the selection function and the contamination level are accurately predicted, the sample can be used for statistical studies.

This work is the extension of the previous SWXCS catalog (Paper I) to the entire *Swift*-XRT archive as of 2012 November, which includes more than 10,000 fields, as opposed to the ~ 300 fields used in Paper I. In addition, we apply for the first time the *EXSdetect* software to the XRT data to achieve better accuracy and sensitivity. The ultimate goal of SWXCS is to provide a large, well-defined catalog of X-ray selected groups and clusters to investigate X-ray properties and perform classical cosmological tests. The paper is organized as follows. In Section 2, we describe the selection of the *Swift*-XRT fields suitable for our serendipitous survey, and describe the identification and classification of the extended sources. In Section 3, we present the SWXCS catalog and compare it

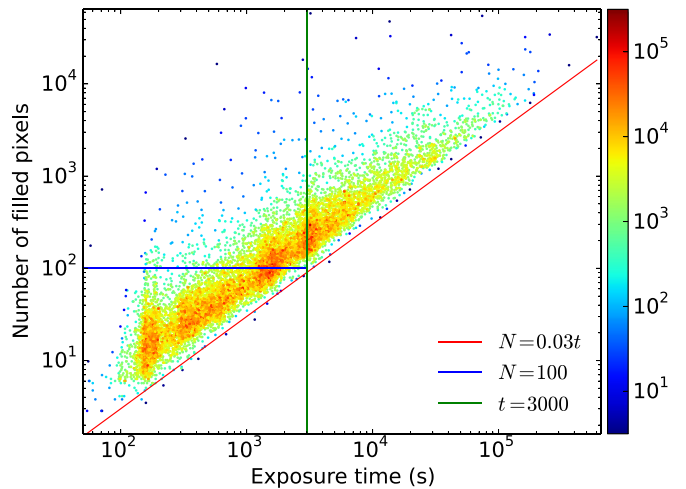


Figure 1. Number of filled pixels (N) in the soft-band image vs. exposure time (t) for each field of the XRT archive as of 2012 December. The red line ($N = 0.03t$) shows the lower envelope of the distribution. The horizontal blue line shows the condition $N > 100$, which ensures a reliable background measurement, while the vertical black line shows the conservative threshold $t_{\text{exp}} > 3000$, which guarantees the condition $N > 100$. Note that the large majority of fields with $t_{\text{exp}} < 3000$ and $N \gg 100$ are dominated by one or few bright sources, therefore, despite the large number of filled pixel, their background is poorly characterized.

with previous works in the field. In Section 4, we compare this catalog to the previous release. In Section 5, we search for counterparts in the optical, X-ray, and Sunyaev–Zeldovich (SZ) catalogs for all our sources. Finally, our findings are summarized in Section 6.

2. FIELD SELECTION AND SOURCE IDENTIFICATION

2.1. Field Selection

From the entire *Swift* XRT archive in the period 2005 February–2012 November, we select all the fields that can be used to build an unbiased, serendipitous X-ray cluster catalog. First, we exclude all of the fields whose Galactic latitude $|b| \leq 20^\circ$. Although these fields could in principle be used to search for bright extended sources, they are typically very crowded, which would cause severe blending problems when the spatial resolution is limited. Moreover, a significant fraction of the soft band emission from groups and clusters would be absorbed by the high H I Galactic column density. The search for the brightest groups and clusters in the Galactic fields will be performed with a different technique in a dedicated paper (A. Moretti et al., in preparation).

Second, we exclude the shallow fields whose exposure time is $t_{\text{exp}} \leq 3000$ s. This limit guarantees $\gtrsim 100$ total photons in the soft band in each field (see Figure 1). This threshold represents the minimum number of photons to sample the background in an X-ray image, which is a critical step to identify extended sources as enhancements of the photon density with respect to the background level. We set a lower limit of 100 to the number of total photons based on extensive simulations of background-only images, where we tested the capability of recovering the true background in our algorithm (see Liu et al. 2013, and the Appendix). This forces us to discard a large number of fields (see lines in Figure 1) which would have contributed only at very high fluxes ($\gtrsim 10^{-12}$ erg cm^{-2} s^{-1}) where the expected number of clusters is very low.

We are also forced to exclude the deepest field (164440+573434), whose exposure is 1.9 Ms. This choice,

which appears to be particularly unfortunate, is due to the large background in the final image. While the internal parameters of *EXSdetect* are optimized for almost the entire range of exposure among our fields, *EXSdetect* becomes unstable when applied to XRT images with exposure times around 2 Ms. Therefore, we choose to discard the field 164440+573434, which would require a different approach with respect to the rest of the survey. We note that the performance of *EXSdetect* in the second deepest field, whose exposure time is 1.1 Ms, has been successfully tested with our simulations.

A further, fundamental step is to filter out all of the fields that are directly targeting groups or clusters of galaxies, since they would clearly introduce a positive bias toward the detection of extended sources. In principle, one can simply excise the targeted group or cluster and use the rest of the field. However, due to the correlation function of dark matter halos, to have an unbiased sample one should also exclude extended sources with similar redshifts. Since this information is not available for many of our sources, we decided to remove all of the fields which, on the basis of the target name and coordinates, are aimed at groups and clusters of galaxies. We also filter out observations targeting nearby galaxies because such galaxies appear as bright extended X-ray sources, whose emission is not associated with ICM but mostly with X-ray binaries and massive star formation events. On the other hand, all of the fields targeting GRBs and active galactic nuclei (AGNs) are included in this survey. In [Paper I](#), we already showed that GRBs show no spatial correlation with galaxy clusters, and AGNs are not expected to be correlated with clusters. It is actually expected that AGNs are suppressed in cluster environments, at least locally ([Khabiboulline et al. 2014](#)). Other multiwavelength studies on the occurrence of AGNs in clusters provide inconclusive results (for example, [Pimblet et al. 2013](#); [Koulouridis et al. 2014](#); [Ehlert et al. 2013](#); [Klesman & Sarajedini 2014](#)). Recently, it has been found that the fraction of luminous AGNs in clusters reaches that in the field in the redshift range $1 < z < 1.5$ ([Martini et al. 2013](#)). Therefore, we conclude that no significant bias in cluster detection is expected from the inclusion of all of the fields targeting AGNs.

The task described above is not straightforward, since the target information in the header of *Swift*-XRT event files is often different from the standard naming conventions or is incomplete. We go through the keywords of target names and coordinates in all of the fields and identify the targets in the NASA Extragalactic Database (NED) when needed. Here we describe the selection rules applied to the *Swift*-XRT archive in order to identify an unbiased subset of fields in detail. Only fields that survived the first triage, i.e., with Galactic latitude $|b| \leq 20^\circ$ and $t_{\text{exp}} \geq 3000$ s, are considered here. For completeness, we also list the excluded fields.

Selected fields:

- 486 GRB follow-up fields, including all the fields previously used in [Paper I](#);
- 698 fields whose targets are found in the NED and are classified as AGNs;
- 654 fields whose targets match an AGN within $5''$ of their coordinates in the NED;
- 22 *Swift*-BAT triggered observations, whose targets are variable hard-X-ray sources;
- 136 fields targeting Fermi/LAT gamma-ray sources (corresponding to header keywords: 0FGL, 1FGL and 2FGL; [Abdo et al. 2010](#); [Nolan et al. 2012](#));

- 71 fields targeting *INTEGRAL* gamma-ray sources (header keyword IGR; [Bird et al. 2004](#));
- 84 fields targeting *ROSAT* detected sources that are not classified as galaxy clusters in NED;
- 401 fields whose target names are found in the NED and are not classified as galaxy clusters or groups;
- 422 fields targeting *Swift*-BAT detected sources (mostly local AGNs);
- 10 safe pointings which are carried out when the telescope loses coordinates; and
- 12 fields targeting pulsars.

Excluded fields:

- 55 fields targeting Abell clusters, the Hydra cluster, Coma, and the Crab Nebula;
- 27 fields targeting the following nearby galaxies: M31, M33, M63, M67, M81, M82, M87, and M100;
- 17 fields targeting comets which may show diffuse X-ray emission;
- 157 fields targeting nearby galaxies cataloged as NGC or Mrk;
- 142 fields within 11° of the Large Magellanic Cloud (LMC) or 6° of the Small Magellanic Cloud (SMC);
- 111 fields targeting supernovae, which are often hosted by nearby galaxies;
- 26 fields targeting Hickson Compact Groups (HCG; [Hickson 1982](#));
- 2 fields targeting *ROSAT* detected sources that are classified as galaxy clusters in the NED;
- 30 fields whose target names are found in NED and are classified as galaxy clusters or groups;
- 9 fields targeting Redshift Survey Compact Groups (RSCG; [Barton et al. 1996](#));
- 52 fields targeting other sources related to clusters in dedicated observational programs;
- 8 fields significantly affected by stray light; and
- 762 fields with unknown target classification.

As previously mentioned, we still have a large number of fields (more than 700) targeting sources whose classification is uncertain. We conservatively discard all of these fields with unknown classification, although many useful fields may be lost with this choice. However, this enables us to avoid any field selection bias, which is a critical requirement for statistical studies and cosmological tests. For consistency with the first SWXCS catalog, we include eight fields that would be excluded with these selection rules (because inside the LMC region) but have been used in [Paper I](#). This inclusion does not have any significant effect on the final catalog. Finally, we select 3004 fields that provide a truly serendipitous sampling of the extragalactic sky. The positions in the sky of the aimpoints of the selected fields are shown in [Figure 2](#).

2.2. Selection of Group and Cluster Candidates

The XRT data reduction is described in [Paper I](#). We consider only the soft-band (0.5–2 keV) images for source detection, since the inclusion of the *Swift*-XRT hard-band images is not useful to identify or to characterize the detected sources.

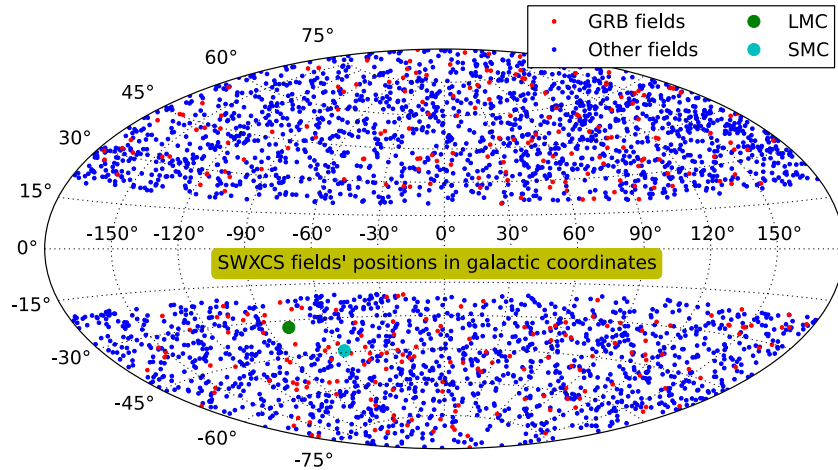


Figure 2. Positions of the 3004 selected fields of the SWXCS. Red points show the GRB fields used in Paper I while the blue points show the new fields used in this work. The positions of LMC and SMC are marked with large dots.

At variance with Paper I where the sources were identified based on a growth curve method, we here use for the first time the *EXSdetect* software. This algorithm and its performance on the *Swift*-XRT data are described in full details in Liu et al. (2013). However, since the software, which is publicly available and currently updated on the SWXCS Web site (<http://www.arcetri.astro.it/SWXCS/> and <http://swxcs.ustc.edu.cn>), evolved significantly in the meantime, we describe in detail in the Appendix the most relevant changes in the current version (v3.0). The first important change concerns the evaluation of the background (see Appendix A.1), while the second concerns the source classification scheme (see Appendix A.2). Another modification introduced in this version is a different treatment of the sources at large off-axis angles ($\theta > 9'$). This is necessary since the in-flight calibration of the *Swift*-XRT PSF shows that at $\theta \sim 10'$ the HEW increases significantly by $\sim 40\%$ (Moretti et al. 2005). Therefore we run *EXSdetect* with a different PSF model to match the expected behavior of the PSF at large off-axis angles only for the source candidates at $\theta > 9'$.

We achieve strong control of the purity and completeness of the sample thanks to extensive simulations. Keep in mind that the simulations are run on a set of synthetic images with the same exposure time distribution and the same background of the selected SWXCS field. Another important aspect is that the input flux distribution of the simulated sources is taken from real, deep data. Point sources are randomly extracted from a distribution modeled on the number counts found in deep *Chandra* fields (Rosati et al. 2002b; Moretti et al. 2003; Xue et al. 2011; Lehmer et al. 2012) and simulated down to a flux about one order of magnitudes lower than the expected detection limit of the SWXCS. The flux distribution of the input extended sources was taken from the number counts of groups and clusters measured in the *ROSAT* deep cluster survey (Rosati et al. 1998). Finally, to take into account the different morphologies of extended sources, we modeled the surface brightness of our simulated sources on real images of 10 bright groups and clusters of galaxies observed with *Chandra*, covering a wide range in ICM temperature (for details see Liu et al. 2013). We simulate 10 times the entire SWXCS survey, which corresponds to $\sim 3 \times 10^4$ X-ray images.

In Figure 3, we show the expected completeness (fraction of extended sources recovered at a given value of input net counts), and the expected number of spurious extended sources expected

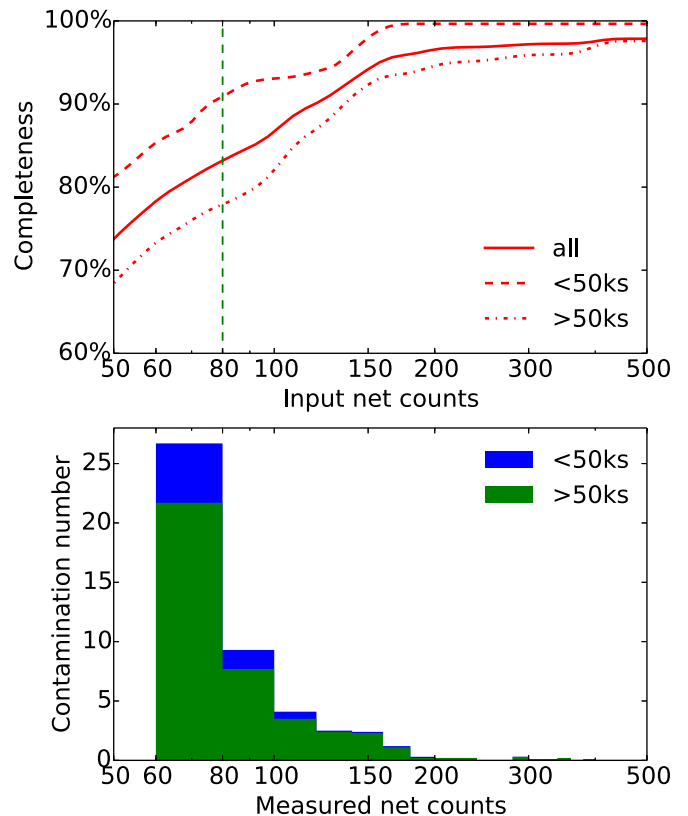


Figure 3. Upper panel: solid red line shows the completeness of SWXCS (defined as the ratio of recovered sources and the number of input sources) as a function of the input net counts as measured with our simulations. The dashed red lines indicate the completeness obtained only considering those fields with an exposure of less than 50 ks (long dashed line) and larger than 50 ks (dot dashed line). Lower panel: histogram of the number of spurious sources expected in the entire SWXCS catalog from our simulations in bins of net detected counts. The different colors show the number of spurious sources found in fields with exposure times above (green shaded area) and below (blue shaded area) 50 ks.

in the entire SWXCS in bins of net detected counts, in the upper and lower panels, respectively. We also plot the completeness and contamination separately for fields with exposure times above and below 50 ks, which account for 10% and 90% of all the fields, respectively. We note that most of the incompleteness and most of the spurious sources come from the 10% deepest fields. The reason for this is the less efficient performance of

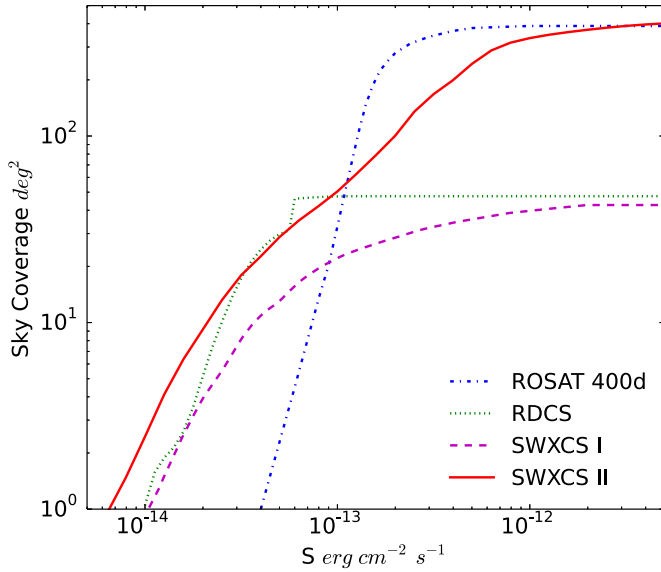


Figure 4. Sky coverage of SWXCS as a function of the soft band flux (solid line). For comparison, we also show the sky coverage of the first release of the SWXCS (Paper I, dashed line), of the *ROSAT* 400d catalog (Burenin et al. 2007, dot-dashed line), and of the RDCS (Rosati et al. 1998, dotted line).

EXSdetect in the presence of high background and crowded fields. For the entire SWXCS, completeness falls below 90% at about 130 net counts, and reaches 83% at 80 net counts. Meanwhile, the contamination number increases rapidly below 80 net counts. Above 80 net counts, the total number of spurious extended sources in the entire survey at any flux is estimated to be about 20, most of which have less than 150 net counts. Therefore, although the completeness is still high and robustly measured below 80 counts, we conservatively set the detection threshold of our catalog to 80 net counts within the source region as defined by the *EXSdetect* algorithm to keep a low number of spurious detections.

For each field, the minimum detectable count rate, computed as $80/t_{\text{exp}}$, corresponds to a position-dependent flux limit obtained by multiplying this number by the field energy conversion factor (ECF) at the aimpoint in the 0.5–2 keV band (which accounts for Galactic absorption and is computed for an average thermal model with a temperature of 5 keV, a metal abundance of $0.3 Z_{\odot}$, and a redshift $z = 0.4$), and by the normalized exposure map, which accounts for the vignetting effects. As shown in Paper I, the ECFs depend weakly on the spectral parameters. Therefore, a flux-limit map is obtained for each field. The sum of the flux-limit maps of the entire set of fields considered in SWXCS provides the sky coverage of the survey as a function of the energy flux (see Paper I). The sky coverage of SWXCS is shown in Figure 4 (solid line). The difference with respect to Paper I (dashed line) at low fluxes is mostly due to the lower threshold used (80 net counts as opposed to 100) and to the fact that several fields are now deeper thanks to new observations targeting fields already included in Paper I. We define the flux limit of the survey S_{lim} as the flux at which the sky coverage falls below 1 deg^2 . This corresponds to a flux of $S_{\text{lim}} = 7 \times 10^{-15} \text{ erg cm}^{-2} \text{ s}^{-1}$, which is fainter than that in Paper I ($\sim 10^{-14} \text{ erg cm}^{-2} \text{ s}^{-1}$). At the bright end, the increase by a factor of 10 is due to the inclusion of the many shallow fields (mostly not associated with GRB) which were not considered in Paper I. The maximum solid angle covered by the survey is $\sim 400 \text{ deg}^2$, reached above a flux of $S \sim 3 \times 10^{-12} \text{ erg cm}^{-2} \text{ s}^{-1}$.

Table 1
Tabulated Values of the Sky Coverage
and of the Completeness as a Function of the
Measured Energy Flux in SWXCS

S ($\text{erg cm}^{-2} \text{ s}^{-1}$)	Sky Coverage (deg^2)	Ratio
3.25e-15	0.1	42.5%
5.15e-15	0.6	50.5%
8.15e-15	1.6	60.4%
1.29e-14	4.4	72.0%
2.05e-14	9.7	80.5%
3.25e-14	18.5	85.6%
5.15e-14	29.6	90.5%
8.15e-14	42.9	95.0%
1.29e-13	64.5	97.6%
2.05e-13	104	99.4%
3.25e-13	171	100%
8.15e-13	319	100%
2.05e-12	372	100%
8.15e-12	409	100%

If we compare the sky coverage of the SWXCS with previous deep X-ray surveys of galaxy clusters, we find that the SWXCS reaches a depth similar to the *ROSAT* Deep Cluster Survey (Rosati et al. 1998) and a width similar to the *ROSAT* 400d survey (Burenin et al. 2007), as shown in Figure 4 (dotted and dot dashed lines). Since the sky coverage is essential for deriving the number counts and eventually, once the redshifts are available, the source number density as a function of redshift, we provide the tabulated values in the second column of Table 1.

The completeness can also be computed as a function of the energy flux simply by computing the flux of each source, which depends on the source counts rate, the ECF in the field, and the actual effective area in the extraction region of the source (see Section 3 for details). The completeness as a function of the flux is then simply obtained as in the previous case, but with computing the ratio of the recovered over the input sources in bins of energy flux. In practice, this is equivalent to convolving the completeness function shown in the upper panel of Figure 3 with the actual distribution of the exposure time, ECF, and effective area of the SWXCS as represented in the simulations. In Figure 5, upper panel, we compare the simulated input extended source distribution with the measured extended source distribution recovered with *EXSdetect* as a function of the energy flux. Note that the input distribution is given by the average of 10 actual realizations of the input model used in the simulations, and therefore it has a 1σ statistical uncertainty, shown by the shaded area. Note also that here the sky coverage is already accounted for. The curve in the lower panel of Figure 5 shows the ratio of output to input source distributions as a function of the measured flux. This function is our best estimate of the completeness of the SWXCS as a function of the energy flux. We find that the completeness correction is relevant below $5 \times 10^{-14} \text{ erg cm}^{-2} \text{ s}^{-1}$, while it is negligible above $10^{-13} \text{ erg cm}^{-2} \text{ s}^{-1}$. We remark that since the completeness is computed as a function of the measured energy flux (and not the actual input flux used in the simulation), this correction also takes into account the effect of the Eddington bias expected in the SWXCS. This function is also tabulated in Table 1, third column. The combination of the sky coverage and the completeness function as a function of the energy flux allows one to derive the SWXCS number counts directly from the catalog (see Section 3).

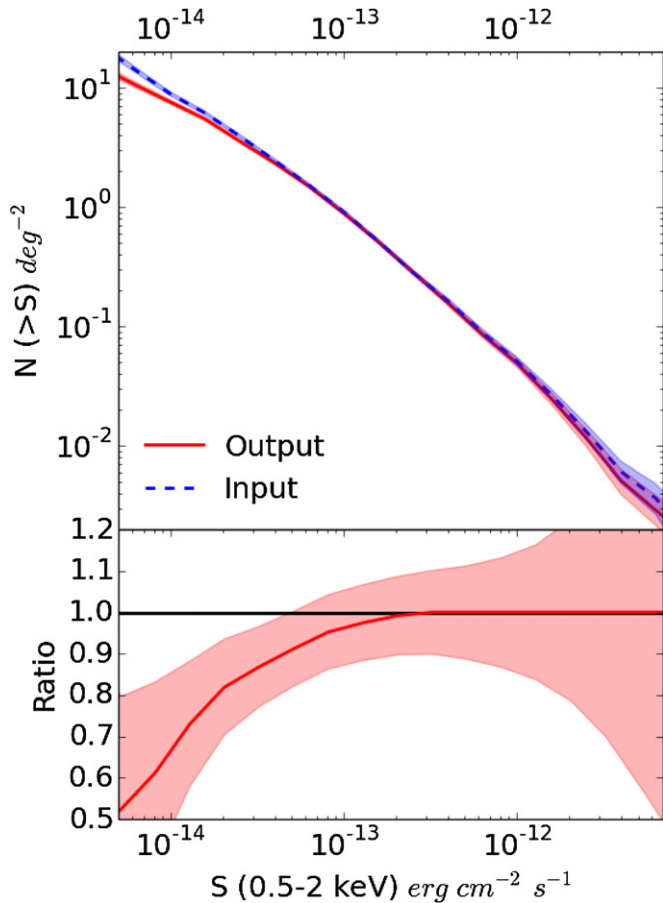


Figure 5. Upper panel: blue dashed line and red solid line show, respectively, the input number counts and the measured number counts from the simulation as a function of the energy flux. Here we used the entire set of simulations (corresponding to 10 times the entire SWXCS survey). Shaded areas show the 1σ uncertainty on the input and recovered number counts. Lower panel: ratio of recovered differential number counts to the input differential number counts, with 1σ uncertainty, as a function of the energy flux. This curve, along with the sky coverage, is used to compute the number counts in SWXCS.

2.3. Filtering of Spurious Sources Not Included in Simulations

By running *EXSdetect* (version 3.0) on the soft-band images of the 3000 fields, we obtain 430 extended source candidates with a soft-band photometry larger than 80 net counts in the source region defined by the *EXSdetect* algorithm itself. According to the expected performance of *EXSdetect*, the directly obtained source catalog should have only about 20 spurious sources. Apart from this budget, however, we know that we have spurious sources associated with circumstances not included in the simulations, but which can be easily identified and filtered out.

The first class of these sources is the piled-up targets, which we can always safely assume to be bright AGNs or GRBs. At the *Swift*-XRT angular resolution, in fact, it is very unlikely that a bright cool core can be affected by pile-up. Clearly, the pile-up effect modifies the shape of the inner regions of unresolved sources, causing the failure of our source classification algorithm based on the comparison of the source profile with the synthetic image of an unresolved source in the same position and with the same flux. For obvious reasons, we did not attempt to include this effect in our simulation. On the other hand, piled-up sources can be easily identified and removed. As a simple and effective criterion for identifying

piled-up sources, we compute the count rate of each source. All of the data we used are observed in Photon Counting mode, which has a time resolution of 2.5 s (Burrows et al. 2005). According to the *Swift*-XRT documents, any source brighter than $0.5 \text{ counts s}^{-1}$ in the 0.2–10 keV full band should be checked for pile-up.⁷ Taking the spectrum of 3C 273 as that of a typical unresolved source, we find that the 0.5–2 keV band contains $\sim 50\%$ of all the photons in the full band. Thus, we flag all of the sources with 0.5–2 keV count rates $> 0.25 \text{ counts s}^{-1}$ inside the extraction region as piled-up candidates. Then, we check their classifications from NED, finding mostly QSOs or galaxies, while none of them, as expected, are associated with clusters or groups. This step allows us to reject 34 extended source candidates as piled-up sources. In addition, some of the GRBs may escape this filter since they can suffer pile-up only in high flux states. Since the identification of all of the GRBs is straightforward, we filter out 18 GRBs which were mistakenly classified as extended sources. A simple visual inspection is performed to check whether we may find truly extended sources overlapping the GRB positions, but we found none.

Nearby ($z < 0.05$) galaxies constitute another source of contamination for our sample. At low redshift, spiral galaxies appear as extended X-ray sources in *Swift*-XRT images, which represent the populations of high-mass X-ray binaries (in the case of recent starburst) or low-mass X-ray binaries in the galaxies. Nearby elliptical galaxies may also show X-ray emission which is related to hot gas in their halo. To identify them, we consider the following galaxy catalogs: the Local Volume Legacy Survey (LVL, Dale et al. 2009), the GALEX Ultraviolet Atlas of Nearby Galaxies (Gil de Paz et al. 2007), and the third Reference Catalog of bright Galaxies (de Vaucouleurs et al. 1991), and select all of the galaxies whose major axis diameter is larger than the half-power diameter of the XRT PSF ($18''$). For these sources, the extended X-ray emission strongly overlaps with the optical extent of the galaxies, as seen in the Digital Sky Survey (DSS) optical images or the Sloan Digital Sky Survey (SDSS) images when available, and therefore is clearly dominated by stellar sources. In some cases, we note some emission beyond the optical extent of the galaxies. This is particularly evident in galaxy pairs. However, in all of the cases where the extended emission may be associated with hot gas around the galaxies, its emission is weak and very hard to decouple from the stronger X-ray emission from the disk or the bulge. In other cases, some small-extent diffuse emission is swamped by a central AGN. For all of these sources, an accurate modeling of the non-thermal X-ray emission is needed before the thermal component can be properly evaluated. Given the very small impact that such contributions would have on our final catalog, all 30 of the extended source candidates associated with nearby galaxies are excluded.

Another kind of spurious detection is caused by bright optical sources (generally stars) whose intense optical/UV emission induces significant spurious charge load in the CCD. Such sources are automatically screened by the *Swift*-XRT pipeline. However, this process often leaves a ring-like signature that is classified as extended by our algorithm but can be immediately spotted by visual inspection. We find and reject 10 of these spurious detections.

Another effect that is not considered in the simulations, for obvious reasons, is associated with the wings of bright clusters which only partially fall in the FOV of the XRT

⁷ See <http://www.swift.ac.uk/analysis/xrt/pileup.php>.

image. By visually inspecting RASS, or *XMM-Newton* images when available, centered on the source position, we identify 11 cases in which the wings of large X-ray clusters have been detected as extended source. The classification of these sources by *EXSDetect* is indeed correct, however, we will not include them in the catalog, since the majority of the cluster emission is, in all of the cases, well beyond the XRT FOV. The clusters responsible of these detections are Coma, A0496, A1285, A1387, A1767, A2199, A2199, A2877b, A3334, A3395 SW, and MCXC J1423.8+4015.

The X-ray images sometimes can be contaminated directly by sunlight, which creates a flare in the light curve and significant diffuse emission at the image borders. By checking the light curve of extended sources at the image borders, we find that the emission of 22 source candidates is actually due to optical flares. These sources are discarded as optical contaminations.

We also find that in 11 cases, our extended source candidates are associated with the position of the nominal target of the *Swift*-XRT observation within a distance of $2'$. Among these cases, nine are bright *ROSAT* X-ray sources, which makes them possible galaxy clusters detected but not identified by *ROSAT* because of its poor spatial resolution. In other words, although the targets of *ROSAT* sources were not identified as clusters (see Section 2.1), they have higher probabilities of being clusters than random objects. The other two targets are galaxies that are not associated with known clusters. Apparently, these last two sources may be allowed in a serendipitous sample. However, the perfect position match ($<6''$) indicates a strong connection between the galaxy targeted by *Swift*-XRT and the X-ray extended source. Also in these two cases, a positive bias is introduced because of the possibility of finding a cluster associated with the targeted galaxy. Overall, although these 11 targeted observations survived our field selection (Section 2.1), they may have higher probabilities of hosting groups or clusters with respect to truly serendipitous observations. Therefore we remove these 11 extended source candidates from the final list.

Finally, we consider a last case that is not treated properly in our simulations. We randomly sampled the number counts of unresolved sources on a solid angle of 400 deg^2 . This is what actually happens for genuinely random fields. However, a significant fraction of fields in the *Swift*-XRT archive target very bright QSOs. In some of these cases, we find anomalous extended sources which are likely to be due to spurious effects associated with the X-ray emission of the bright QSO. In particular, in two fields targeting extremely bright quasars, we find 6 sources in the outskirts which are most likely associated with the anomalous background due to the presence of the bright source. We also find 5 very bright sources that are surrounded by much fainter extended emission. In these few cases, the extended emission component is sufficient to classify these sources as extended, however, the central source is not identified as unresolved, probably due to the contribution of the extended emission, so it is not removed, as is done for all the cases when unresolved sources are embedded in extended emission. These cases should be treated separately, and a PSF deconvolution of the unresolved source emission should be applied before the extended emission can be disentangled from the unresolved emission and properly measured. Since this procedure would introduce large errors to the photometry of the faint extended emission, we decide to remove these sources from the catalog despite the fact that they include extended emission. Clearly, the angular resolution is a strong limitation that hampers us from properly dealing with such cases. Overall, we remove 11

sources due to effects associated with the presence of targeted, very bright unresolved sources.

At the end of this cleaning procedure, we have removed 147 sources due to effects that could not be included in the simulations. In principle, these effects could be implemented in the reduction pipeline with some additional effort. However, in our case, due to the limited number of sources in the SWXCS, a manual check a posteriori is feasible and the automatization of this filtering process is not crucial at this stage of the project. After this step is completed, we are left with 283 group and cluster candidates whose properties are well described by the completeness and contamination function obtained with our simulations.

2.4. Beyond the Software: Learned Visual Inspection

Assuming that we have filtered out any possible source of contamination not included in the simulations, we now deal with a sample with known statistical properties. However, we can extract more information from the simulations. If we revise all of the spurious sources we find in the simulations (several hundreds), then we can understand in most of the cases why the Voronoi algorithm failed. For example, the quite common case of blending of two or more visual sources can be easily associated with a particular pattern in the surface brightness distribution of the spurious source candidate. This visual learning procedure is very effective and in principle could be implemented in the software as a machine learning process, as is now commonly done for data mining in very large surveys. However, the human eye still appears to be the best tool to implement such complex processes. This has been clearly shown by the crowd-sourcing projects proposed by Galaxy Zoo (see Lintott et al. 2011) in past years, which have proven highly successful. It may be very useful, in the future, to set up such a crowd-sourcing astronomical project based on X-ray images.

In our case, given the small size of our source list, we are able to train the eye with simulations and manually apply the filter through direct visual inspection. Twenty sources are flagged as spurious after this step, consistent with the number of spurious sources expected from the simulations (~ 20). Therefore, we decide to include this step in our source classification scheme. In the end, we are left with a final catalog containing 263 source candidates of clusters and groups, whose selection function is shown in Figure 3. After visual inspection, we are confident that the contamination in the SWXCS catalog is reduced to a level which can be safely ignored when deriving the statistical properties of the sample.

3. SWXCS CATALOG

In Table 2, we list the 263 sources of the catalog with their X-ray properties. The sources already presented in Paper I are marked with an asterisk. The catalog contains the following information.

1. Column 1: source name according to the format officially accepted by the IAU Registry in 2013 February. The format is SWXCS JHHMMSS+DDMM.m. This format is different from that used in Paper I, but has already been used in Paper II. Note that for the sources presented in Paper I, we keep the same positions used in Paper II, although the new positions typically differ by $\sim 5''$.
2. Columns 2 and 3: R.A. and decl. coordinates of the X-ray centroid, defined as the weighted median position of the

Table 2
SWXCS Catalog

Name	R.A.	Decl.	t_{eff}	N_{H}	R_{eff}	N_{net}	SNR	Flux
SWXCS J000251–5258.5	0.713858	–52.974476	304043	1.59	39.3	104 ± 17	6.3	0.8 ± 0.1
SWXCS J000315–5255.2*	0.813067	–52.915205	313159	1.59	79.8	1089 ± 43	25.5	8.5 ± 0.5
SWXCS J000324–5253.8*	0.846572	–52.899251	294650	1.59	90.5	1012 ± 43	23.3	8.4 ± 0.5
SWXCS J000345–5301.8*	0.934069	–53.030934	308065	1.61	67.5	362 ± 30	12.2	2.9 ± 0.3
SWXCS J002044–2544.0	5.181310	–25.733882	3272	2.43	217.2	237 ± 19	12.5	180.8 ± 16.2
SWXCS J002114+2059.7	5.309518	20.995620	95736	3.86	69.9	90 ± 14	6.4	2.4 ± 0.4
SWXCS J002437–5803.9*	6.157687	–58.064728	71839	1.22	114.4	360 ± 24	14.7	12.2 ± 1.0
SWXCS J002729–2326.1	6.870954	–23.435391	28798	1.75	99.2	104 ± 13	7.9	8.9 ± 1.2
SWXCS J002824+0927.1	7.098729	9.451710	44478	3.95	99.8	121 ± 15	7.9	7.1 ± 0.9
SWXCS J002826+0918.3	7.110244	9.304376	45409	3.76	102.4	140 ± 16	8.6	8.0 ± 1.0

Notes. Sources marked with an asterisk are included in the first release of SWXCS (Paper I; Paper II). Column 1: source name according to the IAU Registry; sources included in the first release keep the name used in Paper II despite the new centroid positions. Column 2–3: R.A. and Decl. (J2000) coordinates of the X-ray centroid in degrees. Column 4: effective exposure time at the source position in seconds. Column 5: Galactic H I column density in 10^{20} cm^{-2} . Column 6: effective radius R_{eff} in arcseconds; the area of the source region is πR_{eff}^2 . Column 7: net counts in the source region in the 0.5–2 keV band with 1σ error. Column 8: S/N in the 0.5–2 keV band. Column 9: flux in units of $10^{-14} \text{ erg cm}^{-2} \text{ s}^{-1}$ in the 0.5–2 keV band, with 1σ error.

(This table is available in its entirety in machine-readable form.)

27 brightest pixels in the source region (each pixel is weighted by its density which equals to the pixel value divided by Voronoi cell area).

- Column 4: the effective exposure time of each source computed as:

$$t_{\text{eff}} = \frac{\sum n_i}{\sum n_i/t_i}, \quad (1)$$

where i is the index of the filled pixels within the source extraction region, n_i is the photon count in the i^{th} pixel, and t_i is the corresponding value in the vignettted exposure map.

- Column 5: value of the Galactic neutral hydrogen column density in units of 10^{20} cm^{-2} , as found in the Leiden/Argentine/Bonn radio survey (Kalberla et al. 2005).
- Column 6: R_{eff} in arcsec, defined such that πR_{eff}^2 equals the source extraction area (which has no a priori constraints on its shape).
- Column 7: the net counts N_{net} measured in the soft band image by *EXSdetect* inside the source extraction region found by the VT+FOF method, after background subtraction and removal of unresolved sources. At present, no correction is applied to compensate for the lost diffuse emission in the region of the removed unresolved source. The 1σ error is computed as $\sqrt{N_{\text{tot}} + N_{\text{bkg}}}$, where N_{bkg} is the count of background photons and $N_{\text{tot}} = N_{\text{net}} + N_{\text{bkg}}$.
- Column 8: signal-to-noise ratio (S/N) in the soft band, computed as the net counts divided by the associated error.
- Column 9: estimated soft-band flux in units of $10^{-14} \text{ erg cm}^{-2} \text{ s}^{-1}$. To compute the flux for each field, we estimate the ECF in the 0.5–2 keV band, taking into account Galactic absorption in this field, assuming a hot diffuse gas emission model with a temperature of 5 keV, a metal abundance of $0.3 Z_{\odot}$, and a redshift of $z = 0.4$. As shown in Paper I, the ECF depends weakly on the spectral parameters. The flux of each source is calculated as $S = N_{\text{net}} \times \text{ECF}/t_{\text{eff}}$. The 1σ error of flux is measured by propagation considering the error of net counts and a 4% systematic error of ECF due to the typical uncertainty in the actual spectra shape of each source (see Paper I). More accurate fluxes will be available from the X-ray spectral analysis of our sources, which is postponed until a forthcoming paper (A. Moretti et al., in preparation).

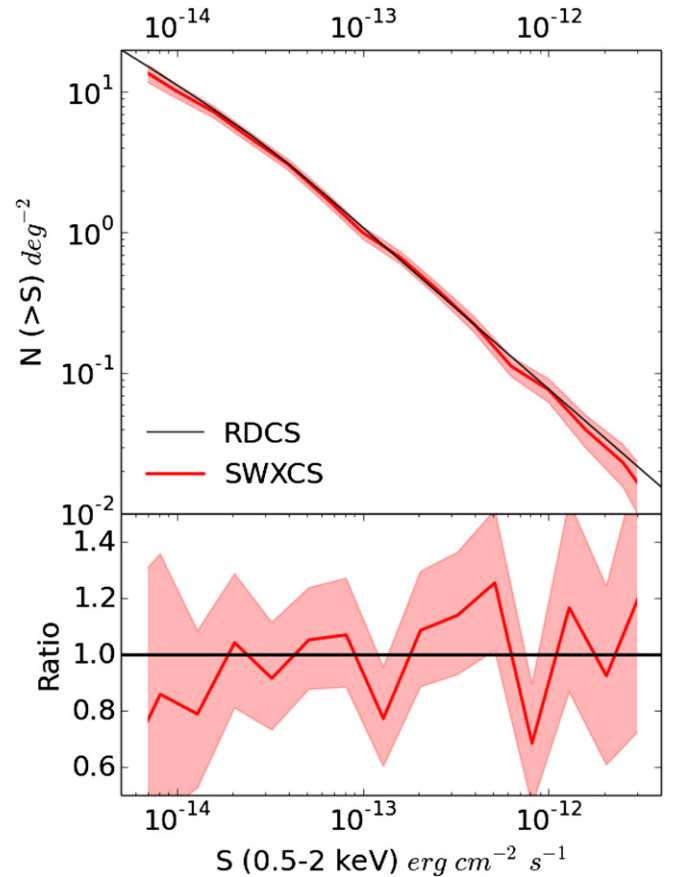


Figure 6. Upper panel: red solid line shows the corrected number counts of SWXCS. The black line is the best-fit double power-law model of RDCS (Rosati et al. 1998). Shaded areas show the corresponding 1σ confidence intervals in both panels. Lower panel: the ratio of SWXCS over RDCS differential number counts.

Finally, using the sky coverage and the completeness function described in Section 2.2, we compute the number counts of the SWXCS catalog following the same procedure as described in Paper I. The corrected number counts are shown in the upper panel of Figure 6 with 1σ confidence intervals, which includes the Poissonian error and the uncertainties on the

average conversion factors. As we also found in [Paper I](#), the number counts are consistent with the $\log N$ – $\log S$ of the *ROSAT* Deep Cluster Survey (RDCS; Rosati et al. 1998; see lower panel of Figure 6). The faint end is also consistent with the very deep number counts measured from the Extended Chandra Deep Field South (A. Finoguenov et al., in preparation). We find that the differential number counts, after correction for incompleteness, can be fit with a broken power law. The best-fit model is

$$\frac{dN}{dS} = \begin{cases} (1.29 \pm 0.26) \times \left(\frac{S}{10^{-13}}\right)^{-2.14 \pm 0.06}, & S > (5.1 \pm 2.0) \times 10^{-14} \\ (1.75 \pm 0.35) \times \left(\frac{S}{10^{-13}}\right)^{-1.68 \pm 0.16}, & S < (5.1 \pm 2.0) \times 10^{-14} \end{cases} \quad (2)$$

where S is in unit of $\text{erg cm}^{-2} \text{s}^{-1}$. Therefore, the slope of the faint end appears to be flatter than the slope at the bright end, although with a low significance ($< 3\sigma$).

4. COMPARISON WITH PAPER I

The first release of the SWXCS catalog ([Paper I](#)) was based on a much smaller number of fields (~ 300 GRB follow-up fields), and was obtained using a standard wavelet detection algorithm coupled with a growth-curve method used to characterize extended sources. To compare this work with the previous release, we first investigate the effect of using *EXSdetect*, which is applied to real data for the first time in this work. After filtering out all of the spurious sources as described in Sections 2.3 and 2.4, *EXSdetect* detects 113 sources in the GRB follow-up fields used in [Paper I](#) (and clearly also included in this work). All 72 of the sources presented in [Paper I](#) except one (SWXCS J022344+3823.2) are recovered by *EXSdetect*. In addition, 42 new sources are detected for the first time by *EXSdetect*. Among the newly detected sources, 17 have less than 100 net counts. The other 25 new sources, instead, have photometry brighter than 100 net counts, and therefore should have been included in the first release of the catalog in [Paper I](#). So we conclude that they were simply missed by the detection method used in [Paper I](#). This shows that the *EXSdetect* algorithm is more efficient, allowing us to recover, above the same photometry threshold, 30% more sources than in [Paper I](#). In the upper panel of Figure 7, we plot the flux distribution of the 113 *EXSdetect* detected sources, compared with the flux distribution of the sources of [Paper I](#). Most of the newly detected sources are found at fluxes below $10^{-13} \text{ erg cm}^{-2} \text{ s}^{-1}$, showing that *EXSdetect* is able to reach higher sensitivity, allowing us to further explore the flux range where medium- and high- z clusters are found (few $\times 10^{-14} \text{ erg cm}^{-2} \text{ s}^{-1}$).

In the lower panel of Figure 7, we show that the photometry obtained with *EXSdetect* is in good agreement with the values found in [Paper I](#) for the 71 sources in common. Note that the fluxes measured in [Paper I](#) are corrected for the missed flux beyond R_{ext} assuming a best-fit β model, while in this work no correction is applied. The best-fit relation between *EXSdetect* fluxes and the fluxes in [Paper I](#) reads as follows:

$$\log\left(\frac{S_{\text{Paper I}}}{10^{-13}}\right) = (0.97 \pm 0.13) \times \log\left(\frac{S_{\text{EXS}}}{10^{-13}}\right) - 0.05. \quad (3)$$

The *EXSdetect* fluxes are somewhat higher than the fluxes measured in [Paper I](#), up to a maximum of $\sim 10\%$ for the brightest sources. On the other hand, our simulations showed that the *EXSdetect* photometry is accurate at the level of $\sim 1\%$ – 2%

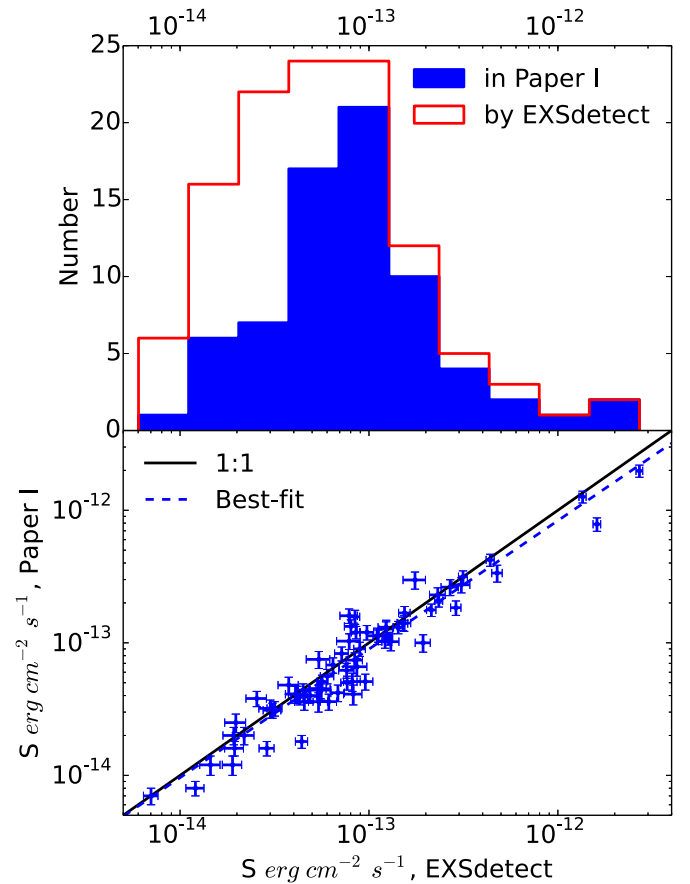


Figure 7. Upper panel: histogram distributions of the *EXSdetect*-measured soft-band fluxes of all the sources detected with *EXSdetect* in the same GRB fields used in [Paper I](#) (red histogram) and of the 71 SWXCS sources already presented in [Paper I](#) (blue filled histogram). Lower panel: for the 71 SWXCS sources that [Paper I](#) has in common, the soft-band fluxes $S_{\text{Paper I}}$ measured in [Paper I](#) within R_{ext} , compared with the soft-band fluxes S_{EXS} measured in this paper with *EXSdetect* from a source region defined by the VT+FOF algorithm. Black solid line shows the relation $S_{\text{Paper I}} = S_{\text{EXS}}$, while the blue dashed line shows the best fit $\log(S_{\text{Paper I}}/10^{-13}) = 0.97 \times \log(S_{\text{EXS}}/10^{-13}) - 0.05$.

(see Figure 10 in Liu et al. 2013). We remind the reader that *EXSdetect* automatically defined irregular extraction regions thanks to the Voronoi algorithm, as opposed to the circular extraction regions defined in [Paper I](#). We generally find that the *EXSdetect* extraction region is larger than the circular region used in [Paper I](#), as shown in Figure 8, by comparing R_{eff} with the extraction radius R_{ext} defined in [Paper I](#) as the radius where the average source flux equals the background level. Note that two sources whose R_{eff} is more than two times larger than R_{ext} do not appear in this figure because of the large, low surface brightness extents associated with these sources, which was not accounted for in [Paper I](#). Therefore, we conclude that the use of the extraction region defined by the Voronoi method is more efficient for recovering the flux in the low surface brightness outskirts of extended sources, providing a more accurate estimate of the total flux.

Finally, for the sources in common, we show the distribution of the displacements between the positions published in [Paper I](#) and the positions measured by *EXSdetect* (see Figure 9). The discrepancy is mostly due to the different definition of the center of the source used in this work and, to a lesser extent, to the larger extraction regions. Despite this, the center of the large majority of the sources is changed by less than $20''$, a value very close

Table 3
Catalog Cross-correlation Results

Name	z_{opt}	z_{TNG}	z_X	Catalog	Cluster Counterpart	Galaxy Counterpart	Separation
SWXCS J000315–5255.2*			0.62 ± 0.1				0.00
SWXCS J000324–5253.8*			0.76 ± 0.01				0.00
SWXCS J002044–2544.0	0.141			Planck	Planck 119		1.22
	0.1410			REFLEX	RXC J0020.7–2542		1.45
	0.1410			MCXC	MCXC J0020.7–2542		1.46
	0.142352			Abell	A0022		2.08
SWXCS J002437–5803.9*			0.195 ± 0.012				0.00

Notes. Column 1: source name; Column 2: optical redshift of cluster or galaxy counterparts, (p) for photometric; Column 3: TNG measured redshift from Paper II; Column 4: X-ray redshift from Paper II; Column 5: catalog where the cluster counterpart is from; Column 6: cluster counterparts; Column 7: galaxy counterparts within 7 arcsec found in NED; Column 8: separation of the matches in arcminutes.

(This table is available in its entirety in machine-readable form.)

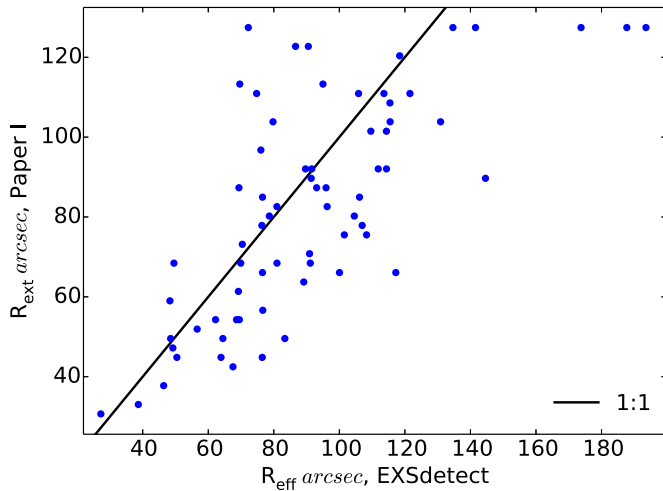


Figure 8. Extraction radius R_{ext} used in Paper I to define the source region, compared to the effective radius R_{eff} for EXSdetect sources. The solid line shows the relation $R_{\text{ext}} = R_{\text{eff}}$.

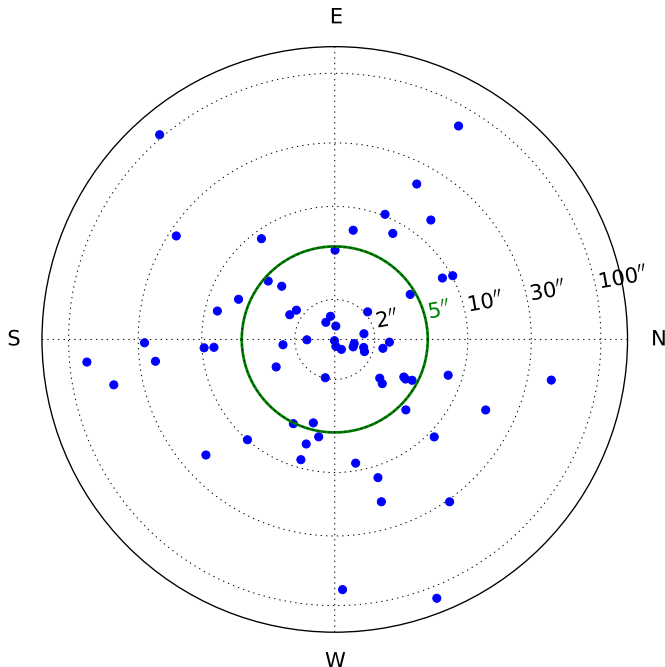


Figure 9. Displacements between the source positions in Paper I and the positions found in this work in units of arcseconds. The green circle shows the median separation corresponding to 5''.

to the HEW of the *Swift*-XRT PSF. Eight sources are found at separations between 0.5 and 2' because of the large extent and the rather flat surface brightness distribution of these sources. Although the change in the nominal position of some source would imply a change in the name according to the IAU format, we prefer to keep the same name used in Paper II for the sources of the first release of the SWXCS catalog.

5. CROSS-CORRELATION WITH OPTICAL, X-RAY, AND SZ CATALOGS AND OPTICAL FOLLOW-UP

We checked for counterparts in previous X-ray cluster surveys, in optical cluster surveys, and in the Planck SZ cluster survey. We simply assume a search radius of 2' from the X-ray centroid, which has been shown to be an efficient criterion in Paper I. Nevertheless, we also inspected the area within 5' from the X-ray centroid to investigate whether some possible identification is found at radii larger than 2'. Counterparts at distances between 2' and 5' are included when the optical or SZ corresponding source has a large uncertainty in position. This is often the case for optical, sparse clusters, or for SZ cluster candidates. We list all of the counterparts associated with the SWXCS sources in Table 3, and we include the measured redshift when available. In case of multiple counterparts, we list all of them. Except for a few cases where we have multiple counterparts with statistically inconsistent redshifts, we keep the counterpart with the smallest distance from the X-ray center.

From optical surveys, we found 233 optical counterparts corresponding to 116 SWXCS sources, including 84 from the SDSS WHL catalog (Wen et al. 2012), 25 from the SDSS AMF catalog (Szabo et al. 2011), 28 from the SDSS MaxBCG catalog (Koester et al. 2007), 45 from the SDSS GMBCG catalog (Hao et al. 2010), 8 from the SDSSC4 catalog (Miller et al. 2005; von der Linden et al. 2007), 27 from the Abell catalog (Abell et al. 1989), 8 from the NSCS1 catalog (Gal et al. 2003), 4 from the NSCS2 catalog (Gal et al. 2003), 3 from the EDC catalog (Lumsden et al. 1992), and finally 1 from the SDSS galaxy groups and clusters catalog built by Berlind et al. (2006). The majority of the SWXCS sources with optical counterparts are listed in more than one catalog. A few WHL counterparts published in Paper II are found with different names in this work because of the updated version of the WHL catalog used here.

From X-ray surveys, we found 70 X-ray counterparts classified as clusters, corresponding to 36 SWXCS sources. In detail, we found 12 X-ray clusters in the *ROSAT* 400d catalog (Burenin et al. 2007), 11 in the Northern *ROSAT* All-Sky (NORAS) catalog (Böhringer et al. 2000), 8 in the *ROSAT*-ESO flux

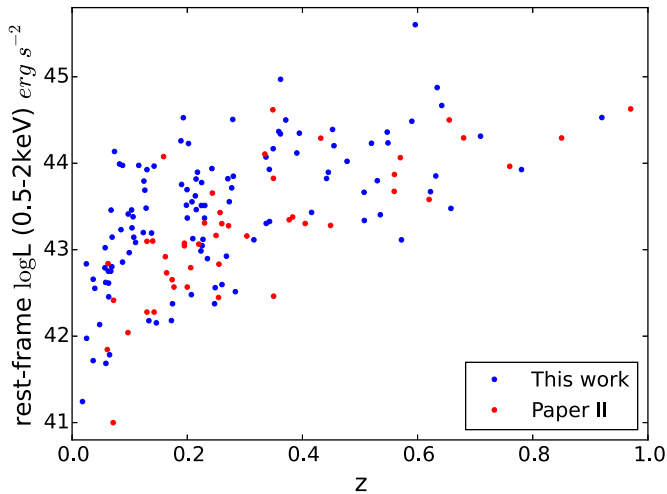


Figure 10. Restframe 0.5–2 keV luminosity vs. redshift. More accurate luminosities measured with X-ray spectroscopy in Paper II are used when available (red points).

Limited X-ray galaxy cluster catalog (REFLEX Böhringer et al. 2004), 3 in the *XMM-Newton* Cluster Survey (XCS) catalog (Mehrtens et al. 2012), and 1 in the *Chandra* Multiwavelength Project (ChAMP) galaxy cluster catalog (Barkhouse et al. 2006). We also found 35 counterparts in the MCXC catalog (Piffaretti et al. 2011), which includes most of the X-ray clusters above.

Finally, for 15 SWXCS sources, we found 16 cluster counterparts detected via the SZ effect, 13 by Planck (Planck Collaboration et al. 2014) and 3 by South Pole Telescope (SPT; Bleem et al. 2014). The Planck sources are typically at larger distances from the X-ray centroid (between 1' and 3') because of the much larger position errors of Planck clusters (see Malte Schäfer & Bartelmann 2007).

Overall, about half (137) of the 263 SWXCS sources were previously identified as groups or clusters of galaxies, while 126 SWXCS sources are new cluster and group candidates. Thanks to these identifications, we are able to recover the redshift information for a significant fraction of our sample. We collect spectroscopic or photometric redshifts for 130 of our sources. Moreover, to increase the number of available redshifts, we also search in NED catalogs for single galaxies with published redshifts not associated with previously known clusters within a search radius of 7'' from the X-ray centroid of

our sources. We find 50 galaxies with measured redshifts for 47 of our sources as a complement to the redshifts obtained from cluster counterparts. In 35 cases where we have both cluster and galaxy counterparts, the galaxy redshifts are consistent with those of clusters. In the 12 cases where no cluster counterpart is found, we tentatively assign the galaxy redshift to our X-ray source.

If we also consider the X-ray redshift derived from the Telescopio Nazionale Galileo (TNG) observations and the X-ray spectral analysis of the sources in catalog I (Paper II), then we have a total of 158 sources with redshifts, from optical spectroscopy or photometry or from X-ray spectral analysis. Therefore, about 60% of our sample has redshift information. For these sources, we plot the restframe 0.5–2 keV luminosities versus redshifts in Figure 10.

We remark that 116 sources overlap with SDSS images. In Figure 11, we show as a sample a selection of SDSS *r*-band images of SWXCS sources with obvious optical counterparts with X-ray contours overlaid. The X-ray and SDSS images (when available) for all of the SWXCS sample can be found in the SWXCS Web site (<http://www.arcetri.astro.it/SWXCS/> and <http://swxcs.ustc.edu.cn>). Among the source with optical redshift, the highest redshift is $z = 0.92$ for XMMXCS J142908.4+424128.9 (Mehrtens et al. 2012). This confirms that the depth of our catalog is sufficient to select clusters up to $z \sim 1$. Another high-redshift source candidate is SWXCSJ011432–4828.4, whose redshift is measured to be 0.97 ± 0.02 from X-ray spectral analysis in Paper II. The presence of clusters at $z \sim 1$ is not unexpected in the SWXCS, given the non negligible sky-coverage of the SWXCS at low fluxes. Based on previous results from the RDCS, we expect of the order of ~ 10 clusters with $z \geq 1$. In addition to the few sources already mentioned, we already identified a sample of high-redshift candidates among the sources with SDSS images but no optical counterparts. As an example, the SDSS images of four of our high- z cluster candidates are shown in Figure 12.

The next step of our project is to increase the number of identifications and redshift measurements, in order to use our sample for statistical studies and cosmological tests. We have started an extensive follow-up program to obtain sensitive, multi-band imaging photometry of the SWXCS sample. Our immediate goal is to measure the integrated properties of the stellar populations of the galaxies through SED fitting. We will also explore the correlation of the galaxy properties with those of

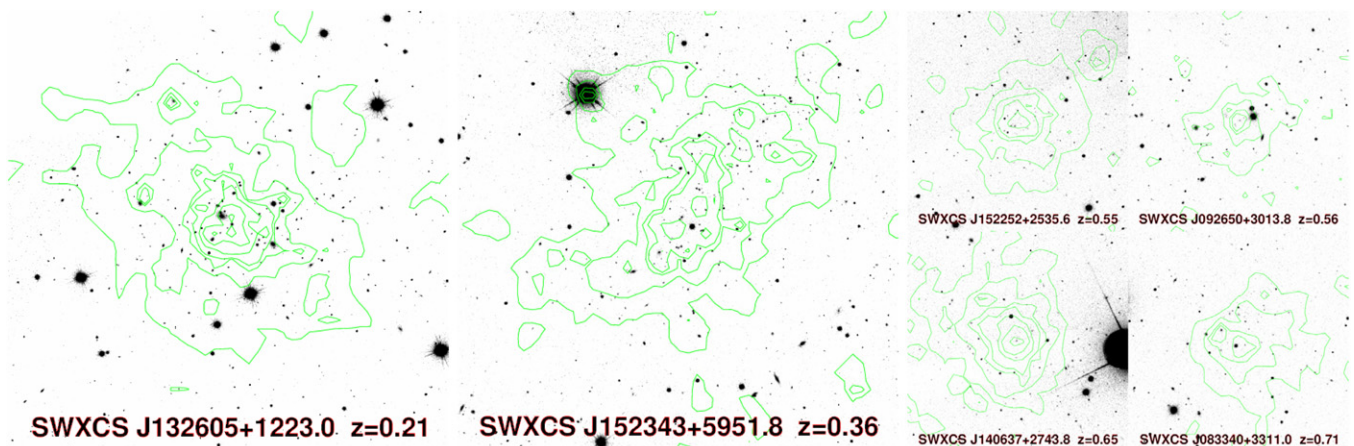


Figure 11. SDSS *r*-band images of a few medium- z SWXCS sources with obvious optical counterparts. The images have sizes of $5' \times 5'$ or $10' \times 10'$. The X-ray contours (green lines) correspond to 2, 5, 10, 30, 70, 150, and 300 times the local background.

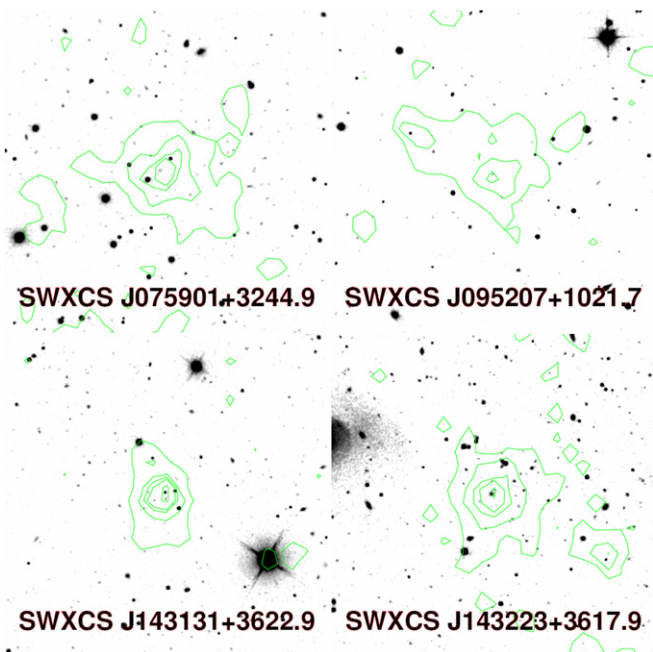


Figure 12. SDSS r -band images of four SWXCS sources with soft-band fluxes less than $5 \times 10^{-14} \text{ erg cm}^{-2} \text{ s}^{-1}$ and without obvious optical counterparts. These sources are among the high- z cluster candidates in the SWXCS. The image sizes are $5' \times 5'$. The X-ray contour generating method is the same as used in Figure 11.

the hosting cluster and their evolution with redshift. The planned observations consist of deep CCD images in the $UBVRiz$ filters which, in the redshift range $0.3 < z < 1$, probe the rest-frame spectral range from mid- and far-UV to optical wavelengths. This choice allows us to properly sample the wavelengths across the 4000 \AA break, which are key for accurate measurements of the integrated stellar mass, star-formation rate, average dust obscuration, and luminosity-weighted age through SED fitting. For the southern sources, we use the Du Pont 2.5 m telescope at Las Campanas Observatory coupled with the Cassegrain-focus Direct Camera. Sources in the northern hemisphere are observed using the Mayall 4 m telescope with the MOSAIC Prime Focus camera at the Kitt Peak National Observatory. Currently, we have observed a total of 41 groups and clusters, 11 in the south and 30 in the north one. We plan to release the reduced and calibrated images and source catalogs of the first year of observations in early 2015. The program will continue throughout the coming years.

We finally note that we can add a significant number of redshifts by extending the X-ray spectral analysis to the entire sample. Although the requirements for a successful identification of the redshifted K_{α} Fe line, as shown in Yu et al. (2011) for *Chandra*, do not apply to most of the SXCS sources, the lower background and the slightly better spectral resolution of XRT allows X-ray redshift measurements in a lower S/N regime, as shown in Paper II. The X-ray spectral analysis of the SWXCS sample will be presented in a forthcoming paper (A. Moretti et al., in preparation).

6. CONCLUSIONS

We search for candidate groups and clusters of galaxies in ~ 3000 extragalactic *Swift*-XRT fields. These fields are selected in order to provide a truly serendipitous survey, and therefore exclude all of the fields in the *Swift*-XRT archive which are somehow correlated with galaxy clusters and groups. We use

the software *EXSdetect*, which was specifically developed for this project and is optimized for detection and photometry of extended sources in *Swift*-XRT images. Therefore, in terms of both covered solid angle and sensitivity, this work constitutes a significant extension of the first SWXCS catalog published in Paper I.

We find 263 X-ray extended sources (including the 71 sources already presented in Paper I) with negligible contamination and a well-defined selection function. The sky coverage ranges from a maximum of $\sim 400 \text{ deg}^2$ to 1 deg^2 at a flux of $0.7 \times 10^{-14} \text{ erg cm}^{-2} \text{ s}^{-1}$. The $\log N$ - $\log S$ is in very good agreement with previous deep surveys. We cross-correlate SWXCS sources with previously published optical, X-ray, or SZ cluster catalogs, finding that 137 sources are already classified as clusters in any of the three bands, while 126 sources are new cluster and group candidates. We already collected redshift measurements (optical, spectroscopic or photometric, and X-ray) for 158 sources (60% of the sample). When the optical follow-up and the extension of the X-ray spectral analysis is completed, the SWXCS will provide a large and well-defined catalog of groups and clusters of galaxies to perform statistical studies of cluster properties and tests of cosmological models. All of the results of the SWXCS are publicly available on <http://www.arcetri.astro.it/SWXCS> or <http://swxcs.ustc.edu.cn>, including machine-readable tables and the *EXSdetect* code.

T.L. and J.X.W. acknowledge support from National Basic Research Program of China (973 program, grant No. 2015CB857005) and the Chinese National Science Foundation (grant No. 11233002, 11421303 and 11403021). T.L., A.M., E.T., and P.T. received support from the “Exchange of Researchers” program for scientific and technological cooperation between Italy and the People’s Republic of China for the years 2013–2015 (code CN13MO5). We also thank the anonymous referee for helpful comments. This research has made use of the NASA/IPAC Extragalactic Database (NED) which is operated by the Jet Propulsion Laboratory, California Institute of Technology, under contract with the National Aeronautics and Space Administration.

APPENDIX

A.1. Background Estimation

The background of an X-ray image is defined as the sum of all the recorded photons not associated with astronomical sources, or associated with some astronomical component that cannot be resolved (like the Galactic diffuse emission). Practically, we divide the photons in an X-ray image into two components: a background component with a roughly constant flux distributed randomly across the whole field, and an additional component associated with single sources with a highly concentrated spatial distribution covering only a very minor fraction of the field. A well-known result, obtained by numerical simulation (Kiang 1966), is that for randomly positioned points, the distribution of the Voronoi cell areas follows an empirical formula:

$$P(\tilde{f}) = e^{-4/\tilde{f}} \left(\frac{32}{3\tilde{f}^3} + \frac{8}{\tilde{f}^2} + \frac{4}{\tilde{f}} + 1 \right), \quad (\text{A1})$$

where P is the cumulative probability distribution function (CDF, $P \in [0, 1]$), $f = 1/a$ is the inverse of the cell area a , called the flux here, and $\tilde{f} = f/\langle f \rangle$ is the flux normalized to the average value $\langle f \rangle = 1/\langle a \rangle$. Therefore, the distribution of the Voronoi cell areas is provided by a function of f with only one

Table 4
Background Estimation Accuracy, Measured by the Ratio (percentage) of Output Flux to Input Flux in the Simulation

Flux	$N = 100$	$N = 1000$	$N = 100000$
Kiang (1966) Formula			
0.001	96.5 ± 6.3	97.4 ± 2.2	97.4 ± 0.2
0.03	95.9 ± 6.4	96.8 ± 2.2	96.9 ± 0.2
0.1	94.2 ± 6.1	95.5 ± 2.0	95.7 ± 0.2
Improved Formulae			
0.001	98.6 ± 6.8	99.7 ± 2.3	99.8 ± 0.2
0.03	98.7 ± 7.0	99.8 ± 2.3	100.0 ± 0.2
0.1	98.6 ± 6.8	100.0 ± 2.2	100.1 ± 0.2

Notes. Three levels of background flux (in unit of photon pixel⁻¹) and three cases of exposure depth (different number of photons within one image) are considered.

parameter $\langle f \rangle$. The value of $\langle f \rangle$ is the background of the image. This relation was used in the first Voronoi algorithm for X-ray source detection proposed by Ebeling & Wiedenmann (1993). Photons in the faintest end of the filled-pixel distribution can be assumed to be only due to the background. Therefore, they proposed an accurate measurement of the average background flux by fitting the faint-end CDF, specifically, only for the $f/\langle f \rangle < 0.8$ part. This part includes $\sim 27\%$ of all the filled pixel in a pure-background image. We made use of this method in *EXSdetect* in Liu et al. (2013). Here we improved the background estimation running Monte Carlo simulations as described below.

We start from a direct test of Equation (A1) with simulations. We randomly distribute one million photons in images of different sizes, chosen in order to have three different flux levels (0.001, 0.03, 0.1 photon pixel⁻¹). Note that float-value positions are assigned to each photon, which is equivalent to assuming an infinitely small pixel scale for the images. Using the *SweepLine* subtask of *EXSdetect*, we construct the Voronoi diagram for each image and calculate the area of each cell. Then, we compare Equation (A1) with the simulated distribution of fluxes. We find that Equation (A1) describes the CDF well in the entire range, but not particularly in the faint end. Therefore, the best fit of Equation (A1) for the $f/\langle f \rangle < 0.8$ part does not recover the average background flux accurately. A systematic deviation is introduced.

Furthermore, the assumption of an infinitely small pixel scale is not realistic. Photon positions in real images are always in integer rather than in float. In other words, digital images always have limited resolutions. The limited resolution induces two effects: a distortion of the CDF in the faint-end due to the lower limit of the Voronoi cell area, and a reduction of data points due to the fact that multiple photons on the same pixel contribute a single Voronoi cell. These effects are flux dependent, and are more significant at high fluxes. In the simulation, we convert the photon positions into pixel positions, and we test Equation (A1) in this realistic situation. As shown in Table 4, the use of Equation (A1) underestimates the average flux by 3%–6% in the flux range 0.001–0.1 photons pixel⁻¹.

The background measurement is improved as follows. We add a parameter c to Equation (A1):

$$P(\tilde{f}, c) = e^{-c/\tilde{f}} \left(\frac{c^3}{6\tilde{f}^3} + \frac{c^2}{2\tilde{f}^2} + \frac{c}{\tilde{f}} + 1 \right). \quad (\text{A2})$$

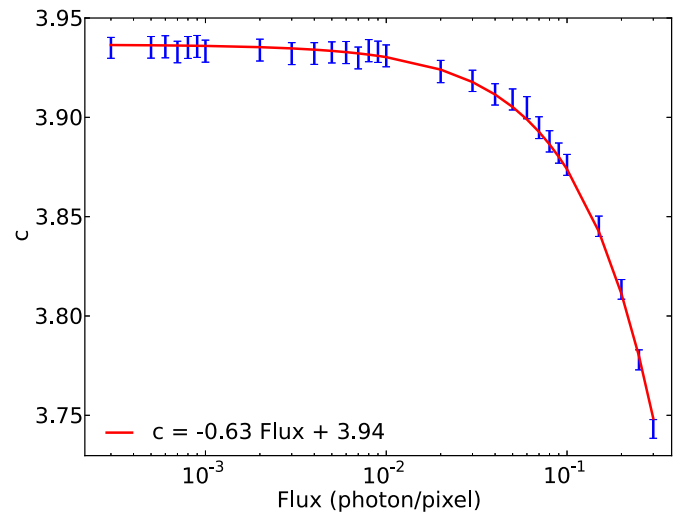


Figure 13. Correlation between the best-fit c parameter in Equation (A2) and the input background. The red line is the best-fit Equation (A3).

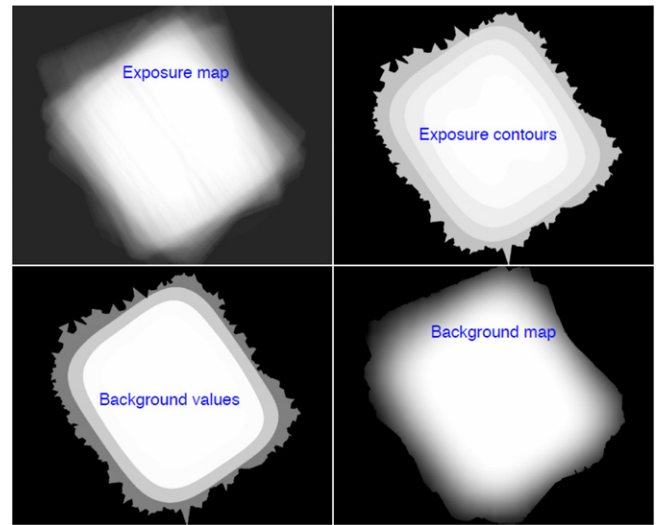


Figure 14. Top left: exposure map of a SWXCS field. Top right: concentric regions are obtained according to the exposure map values. Bottom left: the background is computed in each concentric region by applying Equation (A2). Bottom right: a continuous background image is obtained.

Equation (A2) corresponds to Equation (A1) when $c = 4$. Then, we repeat the fit of the simulated CDF in the region $f/\langle f \rangle < 0.8$ and search for a value of the c parameter which minimizes the difference between the model and the simulated data. We also replace the definition of average flux $\langle f \rangle = 1/\langle a \rangle = N_{\text{pixels}}/\sum a$ with $\langle f \rangle = N_{\text{photons}}/\sum a$, to take into account multiple photons in the same pixel. As shown in Figure 13, we find a linear correlation between c and $\langle f \rangle$:

$$c = -0.63\langle f \rangle + 3.94. \quad (\text{A3})$$

Equations (A2) and (A3) allow us to recover the background accurately with no deviation, as shown in Table 4.

A main limitation of our background measurement method consists of the background variation across the image due to vignetting. In order to take vignetting into account, in Liu et al. (2013), the background map of the field in units of photon pixel⁻¹ was obtained by multiplying the average background flux by the vignetted exposure map. However, only the background from astronomical sources is vignetted,

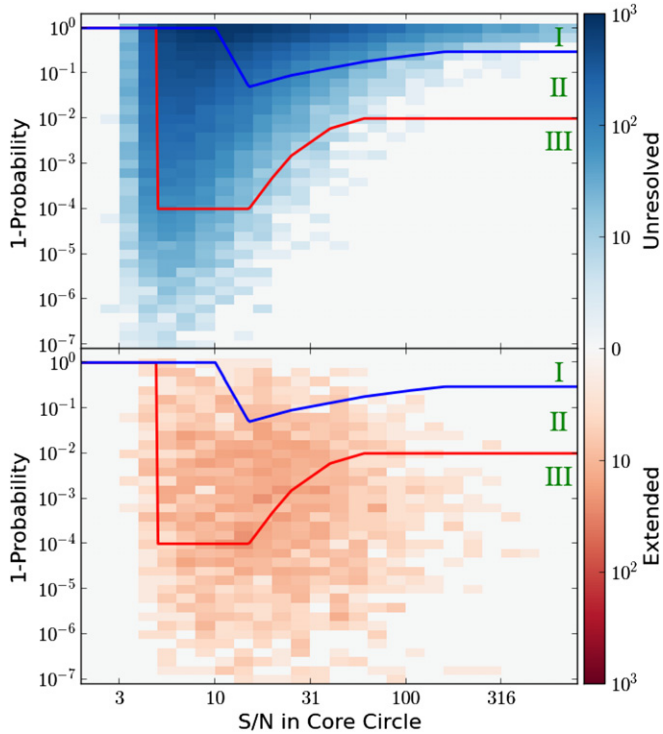


Figure 15. Source classification curves in the $1 - P - S/N$ space, where P is the probability of a given source being extended, based on a comparison between the surface brightness distribution and a PSF model within 5 pixels (see Liu et al. 2013 for details). The selection criteria (blue and red lines) classify the sources into three categories: I = unresolved; II = ambiguous; III = extended sources. The color-coded grid shows the number of simulated sources in the $1 - P - S/N$ space, separately for unresolved (upper panel) and extended (lower panel) sources.

and the background components associated with instrumental noise and cosmic rays vary following a more constant pattern. Therefore, the simple procedure adopted in Liu et al. (2013) over-corrected the vignetting effect, especially at the image borders.

In the new version of *EXSdetect* used in this work, we refined the background estimation in the following way. First, we divide the field into about five concentric regions delimited by the smoothed contours on the exposure map (see upper panels of Figure 14). We calculate the average background flux in each of these regions with the method based on the improved Kiang (1966) formula, creating a step-like background map. Using the background fluxes and exposure times in these bins, we interpolate the relation between the background and the exposure time values in each concentric region with a linear regression. Applying this relation to the original exposure map directly provides a continuous background map (lower panels of Figure 14). The background map is used to recover the background value at the source position when applying the criterion to define source region.

A.2. Source Classification

High angular resolution is a crucial parameter for the detection of extended sources in X-ray images. With HEW of the order of $5''$, it is possible, in principle, to identify any extended source associated with clusters and groups up to high redshifts. The only critical aspect left in high-resolution X-ray images concerns the discrimination of extended features with very low surface brightness from background fluctuations.

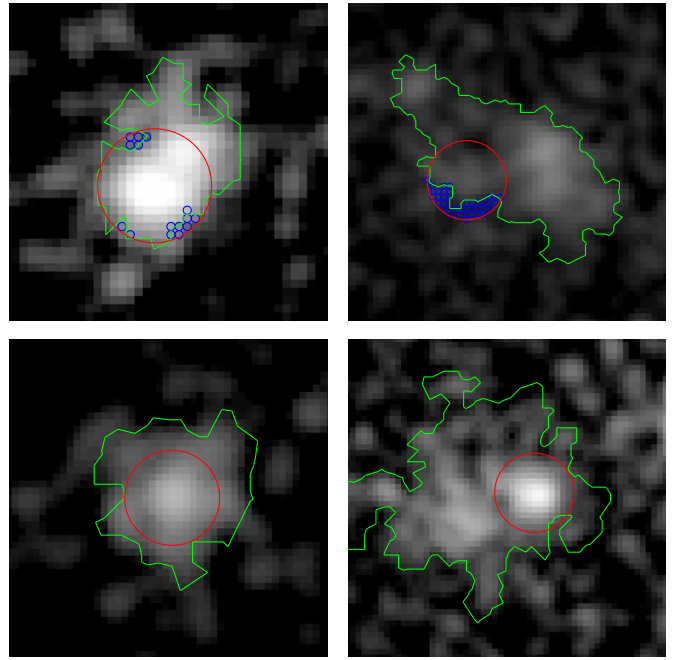


Figure 16. Four examples of disambiguations in real XRT images. Red circles mark the position of the candidate extended source, and have a radius of 7 pixels. Green lines enclose the FOF regions that reach the same flux level as the PSF at a radius of 7 pixels. Blue circles mark pixels outside the FOF regions but inside the red circles. The two sources in the upper panels are classified as unresolved, while the sources in the lower panels are classified as extended.

In Wolter Type I X-ray mirrors, the angular resolution is maximized at the aimpoint, while at large off-axis angles the PSF rapidly degrades. This aspect creates several problems when searching for serendipitous extended sources across an image, particularly if the PSF is not axisymmetric and if the image is obtained by the merging of many exposures.

Swift-XRT has the valuable property, unique among existing X-ray facilities, of showing a constant PSF across the FOV, but the price to pay is a moderate angular resolution. In many cases, the extent of the image of an unresolved source is not very far from the extent of a genuine, compact extended source, like clusters at high- z , cool core small clusters, etc. To minimize this effect, we significantly improved the source classification method of *EXSdetect* with respect to the version of Liu et al. (2013).

In Liu et al. (2013), the source image and the PSF model were compared inside a circle with a radius of 5 pixels (corresponding to a $\sim 60\%$ encircled energy at 1.5 keV) to take advantage of the larger S/N with respect to the outer part of the PSF. In other words, the difference in the profile of the extended source image with respect to the PSF model within $5''$ was sufficient to identify it as extended. Sources were then divided into three types: I unresolved sources, II ambiguous sources, and III extended sources. These selection thresholds were obtained based on our simulations, as shown in Figure 15. In this figure, we show the value $1 - P$, where P is the probability of a source of being extended, corresponding to our selection threshold as a function of the S/N. The density is color coded, in the $1 - P - S/N$ space of the simulated unresolved (upper panel of Figure 15) and of the simulated extended (lower panel of Figure 15) sources.

In the most recent version of *EXSdetect*, we introduce a further step to classify the sources lying between the unresolved and extended regions. We argue that in addition to the profile of the surface brightness distribution, additional information

is contained in the shape of a source. In particular, any unresolved source is expected to have approximately circularly symmetric isocontours according to the PSF model. To recover this information, we consider a larger radius of 7 pixels (corresponding to $\sim 70\%$ encircled energy for an unresolved source). The PSF model clearly provides the flux level of an unresolved source at a radius of 7 pixels. Then, an FOF algorithm is run on all pixels whose flux is larger than the threshold. If the source is truly unresolved, this region should be very close to a circle with a radius of 7 pixels. Significant emission detected outside this radius is taken as a hint of an extended source. On the other hand, if several pixels fall below this value within the circle of 7 pixels, the source is most likely unresolved.

A few cases of source disambiguation are shown in Figure 16. Unresolved sources can be identified with this method even under the contamination of other nearby sources, both brighter and fainter (upper panels of Figure 16). On the other hand, extended sources may be misclassified for several reasons: some may show a very low S/N in the core; some may harbor very compact cores; some others simply harbor a bright unresolved source embedded in the diffuse emission. All of these cases can be identified simply by applying our disambiguation criterion (see lower panels of Figure 16). We tested against simulations that this criterion is efficient when the extended emission is above the background across a region with an effective radius $R_{\text{eff}} \sim 33''$. Clearly, the angular resolution of the instrument constitutes a hard limit below which extended sources cannot be identified by any means. In the case of SWXCS, all of the extended sources with R_{eff} close to the hard limit set by the HEW = $18''$ cannot be identified as extended. Indeed, the minimum size of the sources in the SWXCS corresponds to $R_{\text{eff}} = 27''$.

REFERENCES

- Abdo, A. A., Ackermann, M., Ajello, M., et al. 2010, *ApJS*, **188**, 405
- Abell, G. O., Corwin, H. G., Jr., & Olowin, R. P. 1989, *ApJS*, **70**, 1
- Allen, S. W., Evrard, A. E., & Mantz, A. B. 2011, *ARA&A*, **49**, 409
- Anderson, M. E., Bregman, J. N., Butler, S. C., & Mullis, C. R. 2009, *ApJ*, **698**, 317
- Balestra, I., Tozzi, P., Etori, S., et al. 2007, *A&A*, **462**, 429
- Barkhouse, W. A., Green, P. J., Vikhlinin, A., et al. 2006, *ApJ*, **645**, 955
- Barton, E., Geller, M., Ramella, M., Marzke, R. O., & da Costa, L. N. 1996, *AJ*, **112**, 871
- Berlind, A. A., Frieman, J., Weinberg, D. H., et al. 2006, *ApJS*, **167**, 1
- Bird, A. J., Barlow, E. J., Bassani, L., et al. 2004, *ApJL*, **607**, L33
- Bleem, L. E., Stalder, B., de Haan, T., et al. 2014, arXiv:1409.0850
- Böhringer, H., Schuecker, P., Guzzo, L., et al. 2004, *A&A*, **425**, 367
- Böhringer, H., Voges, W., Huchra, J. P., et al. 2000, *ApJS*, **129**, 435
- Borgani, S. 2008, in *A Pan-Chromatic View of Clusters of Galaxies and the Large-Scale Structure*, ed. M. Plionis, O. López-Cruz, & D. Hughes (Lecture Notes in Physics, Vol. 740; Berlin: Springer), 287
- Borm, K., Reiprich, T. H., Mohammed, I., & Lovisari, L. 2014, *A&A*, **567**, A65
- Burenin, R. A., Vikhlinin, A., Hornstrup, A., et al. 2007, *ApJS*, **172**, 561
- Burrows, D. N., Hill, J. E., Nousek, J. A., et al. 2005, *SSRv*, **120**, 165
- Dale, D. A., Cohen, S. A., Johnson, L. C., et al. 2009, *ApJ*, **703**, 517
- de Vaucouleurs, G., de Vaucouleurs, A., Corwin, H. G., Jr., et al. 1991, Third Reference Catalogue of Bright Galaxies. Volume I: Explanations and references. Volume II: Data for galaxies between 0^h and 12^h . Volume III: Data for galaxies between 12^h and 24^h (New York: Springer)
- Ebeling, H., & Wiedenmann, G. 1993, *PhRvE*, **47**, 704
- Ehlert, S., Allen, S. W., Brandt, W. N., et al. 2013, *MNRAS*, **428**, 3509
- Etori, S., Tozzi, P., Borgani, S., & Rosati, P. 2004, *A&A*, **417**, 13
- Gal, R. R., de Carvalho, R. R., Lopes, P. A. A., et al. 2003, *AJ*, **125**, 2064
- Gehrels, N., Chincarini, G., Giommi, P., et al. 2004, *ApJ*, **611**, 1005
- Gil de Paz, A., Boissier, S., Madore, B. F., et al. 2007, *ApJS*, **173**, 185
- Hao, J., McKay, T. A., Koester, B. P., et al. 2010, *ApJS*, **191**, 254
- Hickson, P. 1982, *ApJ*, **255**, 382
- Kalberla, P. M. W., Burton, W. B., Hartmann, D., et al. 2005, *A&A*, **440**, 775
- Khabiboulline, E. T., Steinhardt, C. L., Silverman, J. D., et al. 2014, *ApJ*, **795**, 62
- Kiang, T. 1966, *ZAp*, **64**, 433
- Klesman, A. J., & Sarajedini, V. L. 2014, *MNRAS*, **442**, 314
- Koester, B. P., McKay, T. A., Annis, J., et al. 2007, *ApJ*, **660**, 239
- Koulouridis, E., Plionis, M., Melnyk, O., et al. 2014, *A&A*, **567**, A83
- Lehmer, B. D., Xue, Y. Q., Brandt, W. N., et al. 2012, *ApJ*, **752**, 46
- Lintott, C., Schawinski, K., Bamford, S., et al. 2011, *MNRAS*, **410**, 166
- Liu, T., Tozzi, P., Tundo, E., et al. 2013, *A&A*, **549**, A143
- Lumsden, S. L., Nichol, R. C., Collins, C. A., & Guzzo, L. 1992, *MNRAS*, **258**, 1
- Malte Schäfer, B., & Bartelmann, M. 2007, *MNRAS*, **377**, 253
- Mantz, A., Allen, S. W., Rapetti, D., & Ebeling, H. 2010, *MNRAS*, **406**, 1759
- Martini, P., Miller, E. D., Brodwin, M., et al. 2013, *ApJ*, **768**, 1
- Maughan, B. J., Jones, C., Forman, W., & Van Speybroeck, L. 2008, *ApJS*, **174**, 117
- Mehrtens, N., Romer, A. K., Hilton, M., et al. 2012, *MNRAS*, **423**, 1024
- Merloni, A., Predehl, P., Becker, W., et al. 2012, arXiv:1209.3114
- Miller, C. J., Nichol, R. C., Reichart, D., et al. 2005, *AJ*, **130**, 968
- Moretti, A., Campana, S., Lazzati, D., & Tagliaferri, G. 2003, *ApJ*, **588**, 696
- Moretti, A., Campana, S., Mineo, T., et al. 2005, *Proc. SPIE*, **5898**, 360
- Moretti, A., Pagani, C., Cusumano, G., et al. 2009, *A&A*, **493**, 501
- Moretti, A., Perri, M., Capalbi, M., et al. 2007, *Proc. SPIE*, **6688**, 66880G
- Nolan, P. L., Abdo, A. A., Ackermann, M., et al. 2012, *ApJS*, **199**, 31
- Piffaretti, R., Arnaud, M., Pratt, G. W., Pointecouteau, E., & Melin, J.-B. 2011, *A&A*, **534**, A109
- Pimblett, K. A., Shabala, S. S., Haines, C. P., Fraser-McKelvie, A., & Floyd, D. J. E. 2013, *MNRAS*, **429**, 1827
- Planck Collaboration, Ade, P. A. R., Aghanim, N., et al. 2014, *A&A*, **571**, A29
- Predehl, P., Andriutschke, R., Böhringer, H., et al. 2010, *Proc. SPIE*, **7732**, 77320U
- Rosati, P., Borgani, S., & Norman, C. 2002a, *ARA&A*, **40**, 539
- Rosati, P., della Ceca, R., Norman, C., & Giacconi, R. 1998, *ApJL*, **492**, L21
- Rosati, P., Tozzi, P., Giacconi, R., et al. 2002b, *ApJ*, **566**, 667
- Schuecker, P. 2005, *RvMA*, **18**, 76
- Szabo, T., Pierpaoli, E., Dong, F., Pipino, A., & Gunn, J. 2011, *ApJ*, **736**, 21
- Tozzi, P., Moretti, A., Tundo, E., et al. 2014, *A&A*, **567**, A89
- Tundo, E., Moretti, A., Tozzi, P., et al. 2012, *A&A*, **547**, A57
- Vikhlinin, A., Kravtsov, A. V., Burenin, R. A., et al. 2009, *ApJ*, **692**, 1060
- Voges, W., Aschenbach, B., Boller, T., et al. 1999, *A&A*, **349**, 389
- Voit, G. M. 2005, *RvMP*, **77**, 207
- von der Linden, A., Best, P. N., Kauffmann, G., & White, S. D. M. 2007, *MNRAS*, **379**, 867
- Wen, Z. L., Han, J. L., & Liu, F. S. 2012, *ApJS*, **199**, 34
- Xue, Y. Q., Luo, B., Brandt, W. N., et al. 2011, *ApJS*, **195**, 10
- Yu, H., Tozzi, P., Borgani, S., Rosati, P., & Zhu, Z.-H. 2011, *A&A*, **529**, A65